Boron-halide Interactions for Crystallization Regulation of 1.68 eV Wide-bandgap Perovskite Prepared via Two-step Method

Shizi Luo,^{ab} Daxiong Liu,^c Xiang Deng,*c Zhuoneng Bi,^b Shuguang Cao,^j Tongjun Zheng,^{ab} Liyao Xiong,^{ab} Hao Li,^d Ning Li,^d Lavrenty G. Gutsev, *ef Nikita A. Emelianov,^e Victoria V. Ozerova,^e Nikita A. Slesarenko,^e Alexander F. Shestakov,^e Sergey M. Aldoshin,^e Gennady L. Gutsev,^g Pavel A. Troshin, *he Bochuan Yang*i Zhibo Zhao,^c and Xueqing Xu, *ab

- ^a School of Energy Science and Engineering, University of Science and Technology of China, Hefei, 230026, P.R. China
- ^b Key Laboratory of Renewable Energy, Guangdong Provincial Key Laboratory of New and Renewable Energy Research and Development, Guangzhou Institute of Energy Conversion, Chinese Academy of Sciences, Guangzhou 510640, P.R. China
- ^c Guangdong Mingyang Thin Film Technology Co., Ltd, Zhongshan, P.R. China
- ^d Institute of Polymer Optoelectronic Materials and Devices State Key Laboratory of Luminescent Materials and Devices, South China University of Technology, Guangzhou, 510640, P. R. China
- ^e Federal Research Center for Problems of Chemical Physics and Medicinal Chemistry of RAS, Semenov Prospect 1, Chernogolovka, 142432, Russia
- f Institute for Micromanufacturing, Louisiana Tech University, Ruston, LA 71272, United States
- g Department of Physics, Florida A&M 711 University, Tallahassee, Florida 32307, United States
- h Zhengzhou Research Institute of HIT, 26 Longyuan East 7th, Jinshui District, Zhengzhou, Henan Province 450000, PR China
- ⁱ Risen Energy Co., Ltd, Ningbo, Zhejiang Province 315609, PR China
- ^j School of Materials Science and Engineering, Henan Polytechnic University, Jiaozuo, Henan 454000, PR China

* Corresponding authors.

E-mail addresses:

xuxq@ms.giec.ac.cn (X. Xu);

Keywords: Tris(pentafluorophenyl)borane, Crystallization regulation, Nonradiative recombination, Two-step Method, Wide-bandgap perovskite

1. Materials

Dimethylformamide (DMF, >99%), dimethyl sulfoxide (DMSO, >99.5%), chlorobenzene (CB, anhydrous, 99.8%) were purchased from Sigma-Aldrich. Isopropyl alcohol (IPA, anhydrous, 99.8%) was purchased from Acros. The NiO_x powder, lead iodide (PbI₂, 99.999%) and lead bromide (PbBr₂) were purchased from Advanced Election Technology Co., Ltd. CsI, [6,6]-Phenyl-C₆₁-butyric acid methyl ester (PCBM), 2,9-Dimethyl-4,7-diphenyl-1,10-phenanthroline (BCP), methylammonium chloride (MACl), formamidinium iodide (FAI) and methylammonium bromide (MABr) were purchased from Xi'an Yuri Solar Co., Ltd. [4-(3,6-Dimethyl-9H-carbazol-9-yl)butyl]phosphonic Acid (Me-4PACz) was purchased from Acros (TCI). MgF₂ was purchased from (Alfa Aesar). Tris(pentafluorophenyl)borane (BCF) was purchased from Aladdin.

2. Fabrication of single junction wide-bandgap perovskite solar cells

The ITO-coated glass substrates (purchased from Wuhan Lattice Solar Energy Technology Co. LTD.) were ultrasonically cleaned with soap solution, deionized water, ethanol and isopropyl alcohol each for 20 min, respectively, and then dried under a stream of nitrogen. The pre-cleaned ITO/glass substrates were treated with UV-Ozone (UVO) for 15 min to remove the organic residue. The NiO_x nanoparticle solution (10 mg/mL) was spin-coated onto the ITO/glass substrates at 2000 rpm for 30 s and annealed for 10 min at 150°C, then quickly transferred to a glove box. Me-4PACz (0.5 mg/mL in ethanol) was spin-coated on NiO_x at 4000 rpm for 30 s, annealed for 10 min at 100°C and cooled for 5 min.

1.5 M PbX₂ (X=I and Br, and the molar ratio of I:Br is 0.75:0.25) powder and 0.060 M CsI were added in mixed solvent (DMF and DMSO with volume ratio of 9:1) to form an inorganic salt solution with 0.015 M RbCl as auxiliary crystallization additive. And the inorganic salt solutions without or with BCF as control or target samples were dropped onto the HTL and spin-coated at 2500 rpm for 30 s, respectively, then annealed

for 1 min at 70°C. The FAI/MABr/MACl (90:9:9 mg) organic salts solution in 1 mL IPA was dynamically dropped onto the PbX₂ film after 5 s of the process starting at 3500 rpm for 35 s, and then annealed for 30 min at 100°C in the N₂ glove box. For post-treatment, 1 mg/mL PEAI in IPA solvent was dynamically spin-coated onto the perovskite surface with 4000 rpm for 30 s, and then annealed for 5 min at 100°C. Next, 20 mg/mL PCBM in CB and 0.5 mg/mL BCP in IPA were spin-coated at 2000 rpm and 4000 rpm for 30 s, respectively. Finally, the Ag top electrode (100 nm) was deposited by thermal evaporation in vacuum through a shadow mask defining the device active area as 0.048 cm².

3. Fabrication of Si bottom solar cells

Silicon heterojunction (SHJ) bottom solar cells were made from 300 μm thick floatzone (FZ) n-type crystalline silicon (c-Si) wafers. Both sides of the wafer were treated with alkaline solution for textured surfaces. Afterward, the wafers were cleaned in RCA solutions and dipped in hydrofluoric acid to remove the silicon oxide layer. ~5 nm intrinsic a-Si:H, ~5 nm n-type, and 15 nm p-type a-Si:H were deposited by plasmaenhanced chemical vapor deposition (PECVD). ITO layers were sputtered from an In₂O₃ target onto both sides of cells, with 20 nm acting as the recombination layer and 100 nm on the rear contact through a shadow mask to define 1.1 cm x 1.1 cm square cells. A 250 nm thick Ag was thermal evaporated through the same shadow mask on the rear surface. Finally, the wafers were laser-cut into 2 cm x 2 cm square substrates for tandem fabrication.

4. Fabrication of Perovskite/silicon two-terminal monolithic tandem solar cells

The processes for postt-reatment are the same as that on single-junction perovskite devices, with a few adaptations:

1) The ${
m NiO_x}$ nanoparticle solution (10 mg/mL) was spin-coated onto the ITO/Si substrates at 4000 rpm for 30 s and annealed for 10 min at 150°C

- 2) The PbX₂ precursor solution with an enhanced concentration from 1.5 to 1.8 M was conducted to completely cover the texture silicon substrate. The mass concentration of the FAI/MABr/MACl (90:9:9 mg) organic salts solution in 1 mL IPA was enhanced to 100:10:10 mg/ml.
- 3) The C60 ETL layer thickness is 15 nm to reduce the parasitic absorption in the top cell.
- 4) The 10 nm SnO₂ was then deposited by atomic layer deposition (ALD) with N₂ as the gas carrier. During ALD deposition, the substrate temperature was maintained at 70 °C and tetrakis(dimethylamino)tin(IV) (TDMASn) precursor source at 60 °C and the H₂O source at room temperature. The dosing and purging time for TDMASn is 0.05 and 10 s, and for H₂O is 0.02 and 6 s. 90 cycles were performed.
- 5) After the SnO₂ layer, a 40 nm IZO layer was then sputtered with 60 W power (3-inch target) on top of the In₂O₃ target, and 150 nm of Ag fingers and busbars were thermally evaporated on top of the IZO. Finally, a 100 nm MgF₂ layer through thermal evaporation was used as the antireflective coating (the device active area as 1 cm²).

5. Characterizations

The perovskite films were characterized by X-ray photoelectron spectroscopy (XPS, ESCALAB 250Xi, Thermo Scientific K-Alpha). Ultraviolet photoelectron spectra (UPS) were also measured by Thermo Scientific ESCALAB 250Xi, with the HeI (21.22 eV) emission line employed for excitation. The surface microstructure of perovskite films and the cross-sectional images of PSCs were obtained using SU-70 high-resolution analytical SEM (Hitachi, Japan). PL and TRPL spectra of perovskite films were obtained using Edinburgh fluorescence spectrometer (FLS980). The X-ray diffraction (XRD) patterns of perovskite films were obtained using X'Pert PRO MPD

X-Ray diffractometer with Cu K α irradiation at a scan rate (2 θ) of 0.0167 ° S⁻¹. For *J-V* measurements, the intensity of the light was 100 mW cm⁻² (simulated AM 1.5 G) provided by ABET Sun 3000 solar simulator and calibrated by a standard silicon reference cell. Grazing incidence X-ray diffraction (GIXRD) was performed using Rigaku SmartLab. Atomic force microscopy (AFM) measurements were performed by Bruker Multimode. The IR s-SNOM measurements were carried out using a neaSNOM microscope (Neaspec, Haar, Germany) in PsHet mode with a Mid-IR laser MIRcat-2400 (Daylight Solutions, USA) installed inside the MBraun glove box (O₂, H₂O < 0.1 ppm). The *J-V* curves, space charge-limited current (SCLC) measurements for the solar cells were performed using Autolab TYPE II electrochemical work station. The external quantum efficiency (EQE) spectra of the solar cells were obtained using QTest Hifinity 5 (Crowntech, USA).

6. Density Functional Theory Calculations and Nonadiabatic Molecular Dynamics

To simulate a BCF-passivated perovskite surface we employed the Vienna Ab initio Simulation Package (VASP) [1]. Initial momentum-space sampling was carried out at the Gamma-point, followed by a more refined $2\times2\times1$ k-point mesh. The calculations utilized the PBE functional with D3 dispersion corrections [2, 3]. Projector augmented-wave (PAW) pseudopotentials were implemented, and the plane-wave energy cutoff was set to 520 eV. Additionally, non-spherical gradient contributions within PAW spheres were incorporated to enhance the accuracy of computed observables, particularly for perovskite oxides [4-6]. We employed relatively large supercell slabs, consisting of $3\times3\times5$ α -FAPbI₃ unit cells, to effectively prevent interactions between passivants and their periodic images. We consider the *x*-axis as the axis perpendicular to the surface, in this context it is the (100) direction. To further minimize spurious interactions, a 20 Å vacuum layer was introduced in the positive *x* direction. Atomic positions and lattice constants were fully relaxed while keeping the overall cell volume fixed. Both the passivated and unpassivated FAI-rich and PbI₂-rich surfaces were considered, and their adsorption energies were calculated as:

$$E_{ads} = E_{surf/pass} - E_{surf} - E_{pass} \#(1)$$

where E surf/pass is energy of the passivator and the surface, E surf and E pass are the energies of the surface and passivator, respectively. Since we were interested in the BCF-I⁻ complex, we also performed a calculation first with BCF and interstitial iodine on the (100) α -FAPbI₃ surface allowing both the lattice and atomic positions to relax. Next, we repeated this calculation with a single negative charge and allowed the atomic positions to relax. This was done because for charged surfaces only a fixed unit cells may be optimized.

Theoretical modelling of the molecular structures and the formation energies of MABr-BCF and FAI-BCF complexes was performed using PRIRODA software [7] using PBE density functional [8], SBK pseudopotential [9] and extended basis for valence electrons. The magnetic shielding constants were simulated using full-electron extended $\Lambda 2$ basis set of cc-pVTZ quality [10]. All calculations were performed at the Supercomputer Center of the National Research Center "Kurchatov Institute".

7. Figures and tables

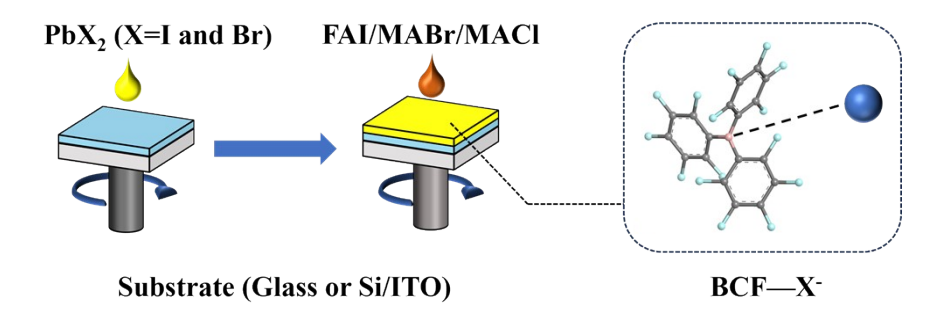


Fig. S1 Schematic diagram of the wide-bandgap perovskite solar cell device fabricated by the two-step process under the regulation of BCF.

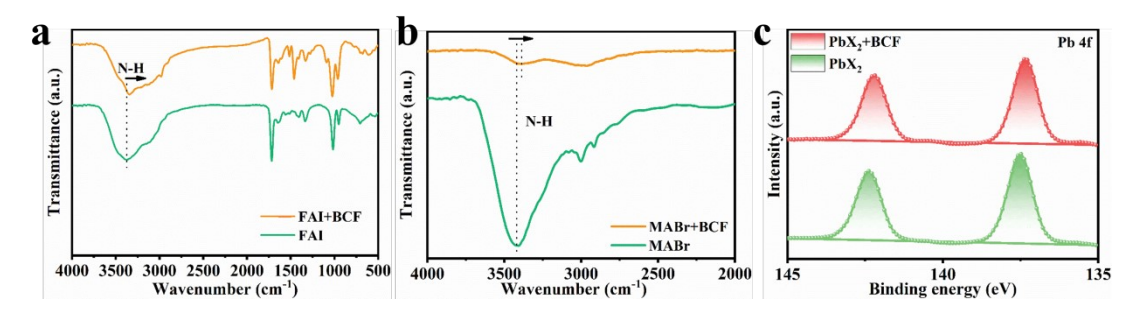


Fig. S2 FTIR spectra of (a) FAI and FAI+BCF mixture, (b) MABr and MABr+BCF mixture, respectively. XPS spectra of (c) Pb 4f for PbX₂ and PbX₂+BCF films.

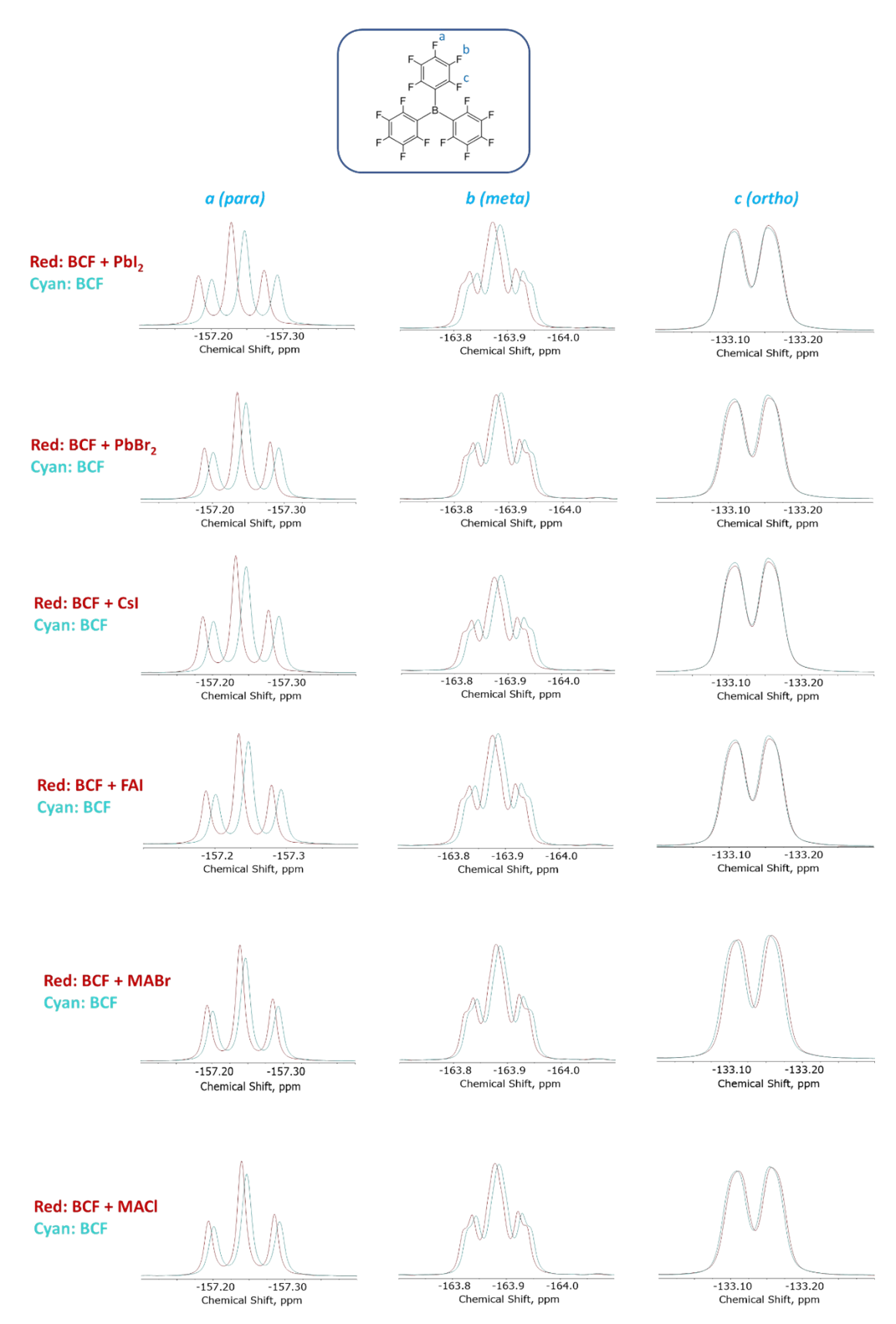


Fig. S3 Evolutions of the peak position in the ¹⁹F NMR spectra of BCF upon interaction with different perovskite precursor components (equimolar mixtures of components dissolved in DMSO-d6).

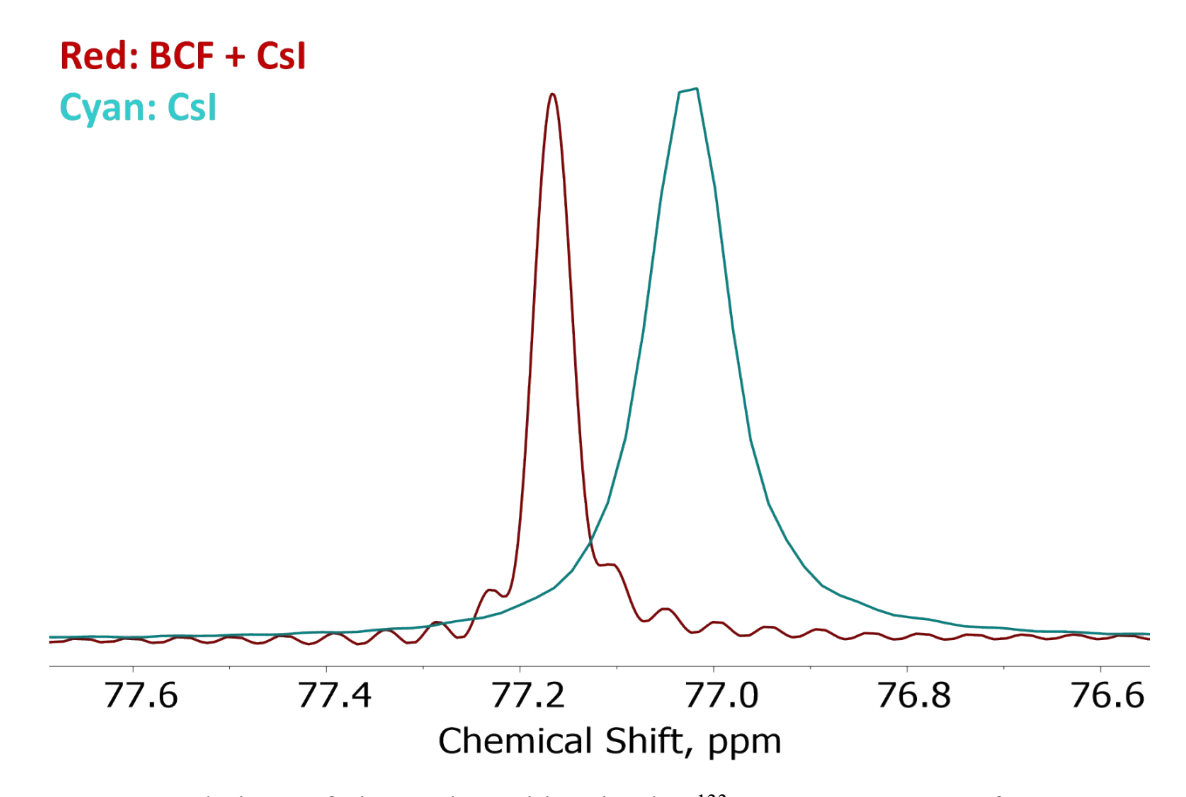


Fig. S4 Evolutions of the peak position in the ¹³³Cs NMR spectra of CsI upon interaction with BCF (equimolar mixtures of components dissolved in DMSO-d6).

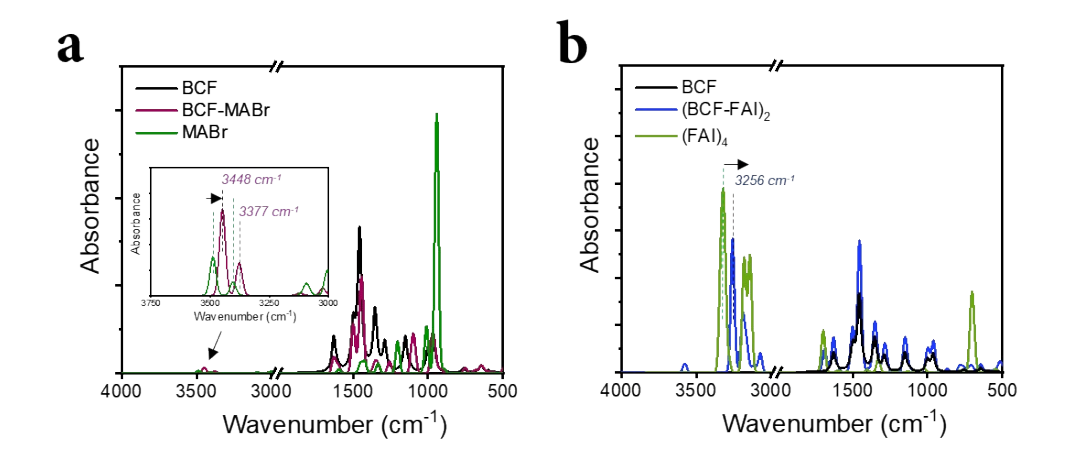


Fig. S5 Comparison of the simulated FTIR vibrational spectra of BCF, MABr and MABr+BCF complex (a) and BCF, FAI (represented by tetramer) and FAI-BCF complex (b).

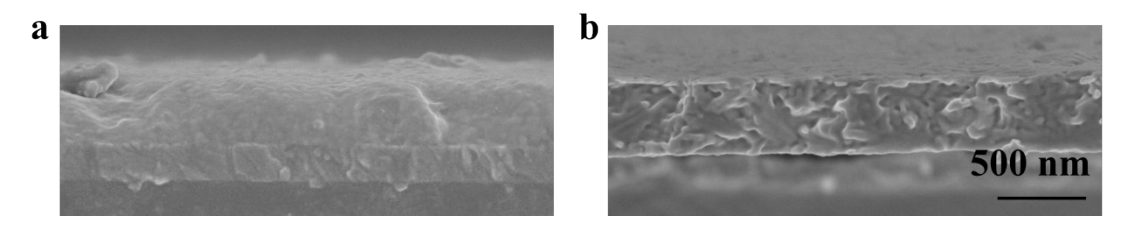


Fig. S6 The cross-sectional SEM images of the PbX_2 (a) and $PbX_2 + BCF$ (b) films.

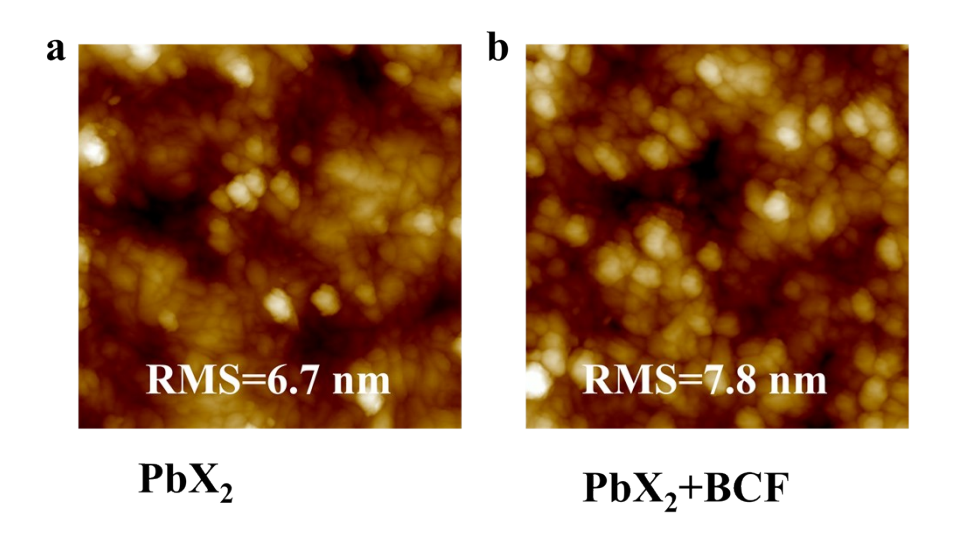


Fig. S7 AFM images of the PbX₂ and PbX₂+BCF films (scale size of 5 μ m×5 μ m).

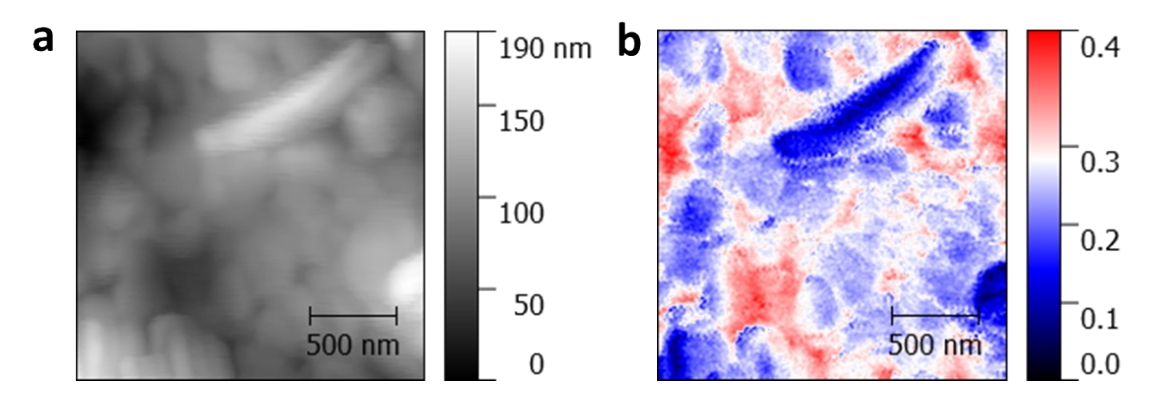


Fig. S8 AFM topography (a) and IR s-SNOM mapping image at 1102 cm^{-1} showing the BCF distribution (red color) within the PbX₂+BCF film (b).

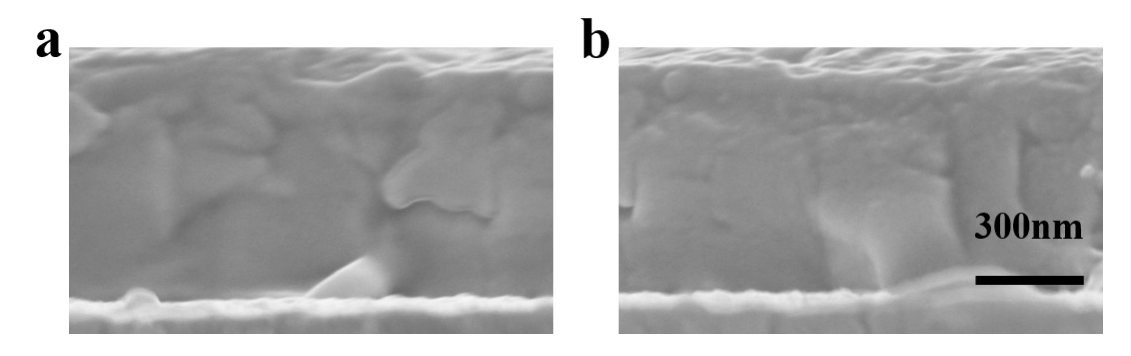


Fig. S9 The cross-sectional SEM images of the Control (a) and Target (b) perovskite films.

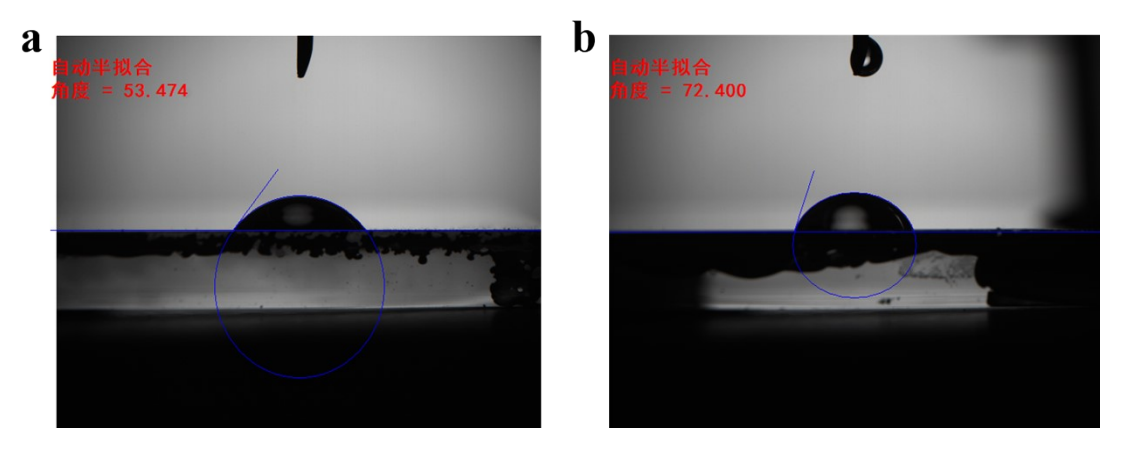


Fig. \$10 The water contact angle of the Control (a) and Target (b) perovskite films.

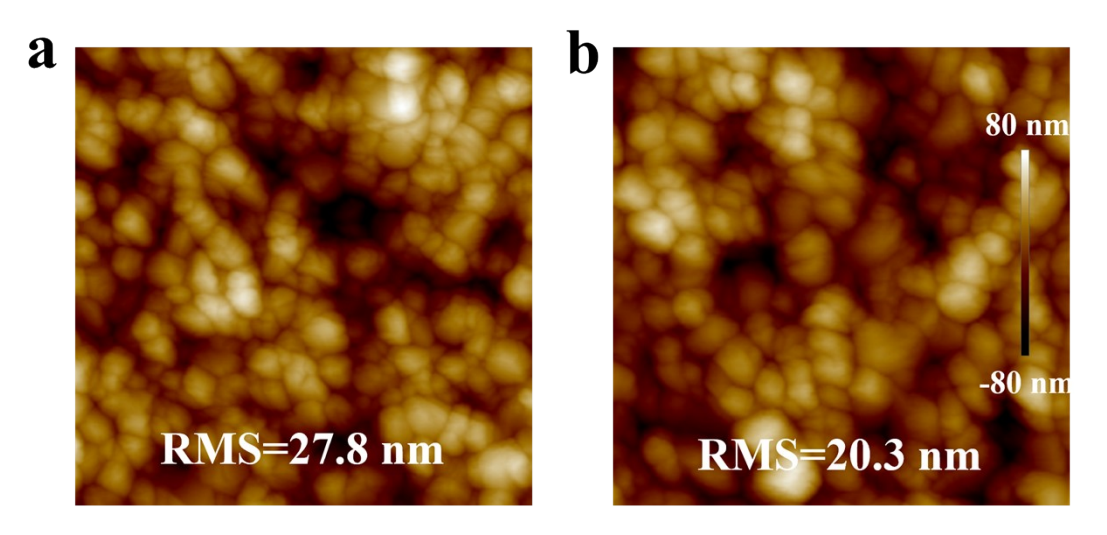


Fig. S11 The AFM images of the Control (a) and Target (b) perovskite films $(5 \times 5 \text{ um}^2)$.

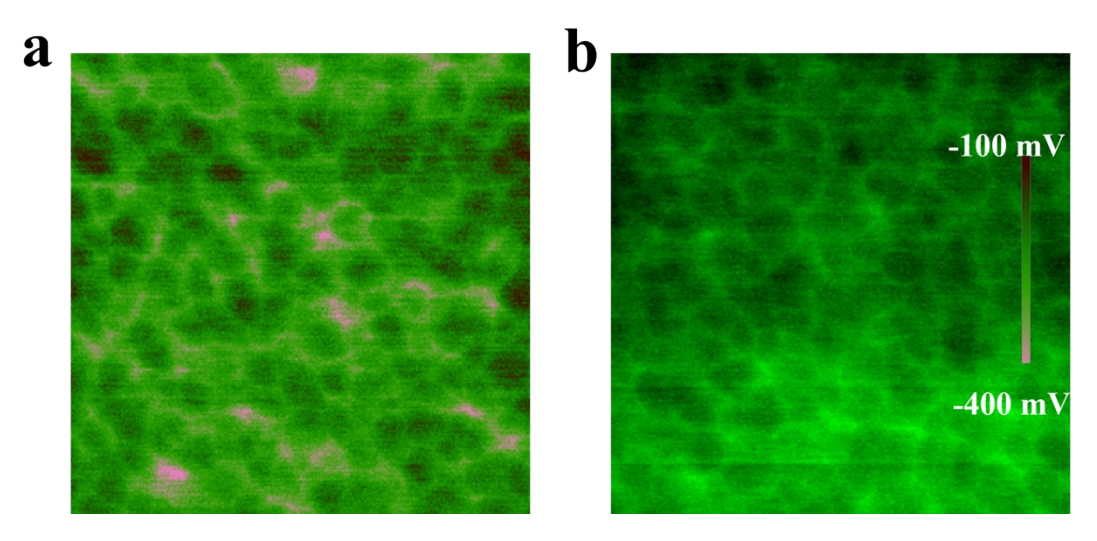


Fig. S12 The KPFM images of the Control (a) and Target (b) perovskite films $(5\times5$ um²).

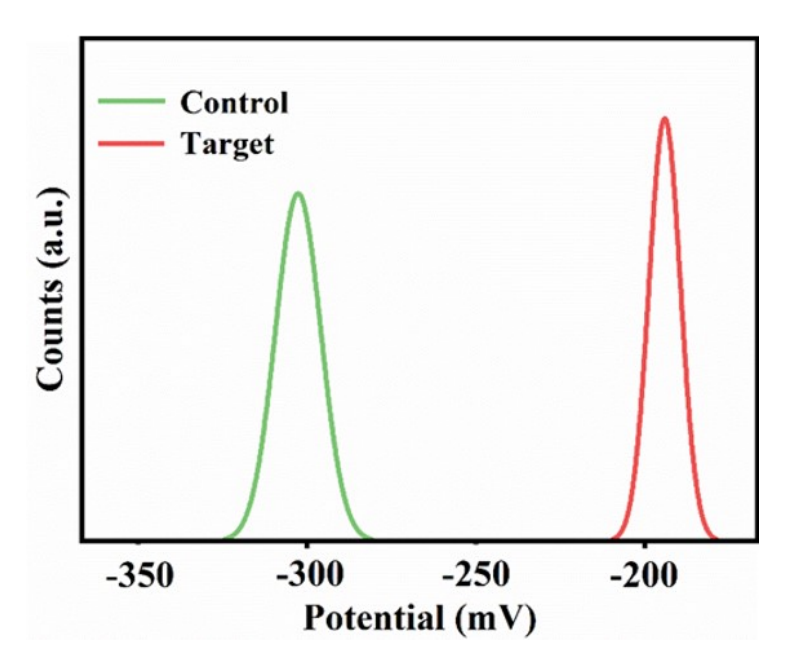


Fig. S13 The surface contact potential distribution of the Control and Target perovskite films.

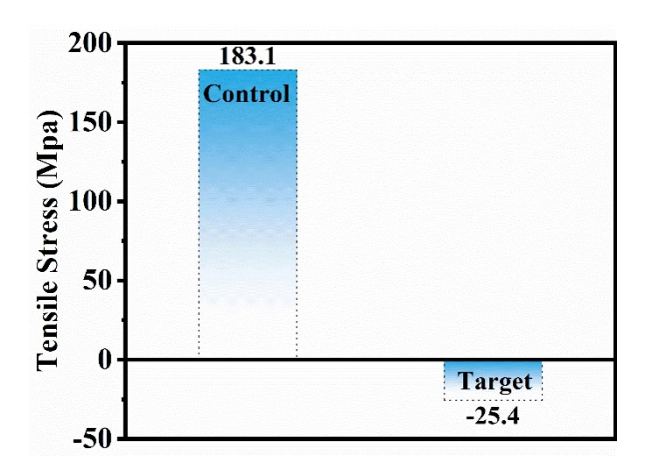


Fig. S14 The illustration shows calculated residual stress of the Control and Target perovskite films.

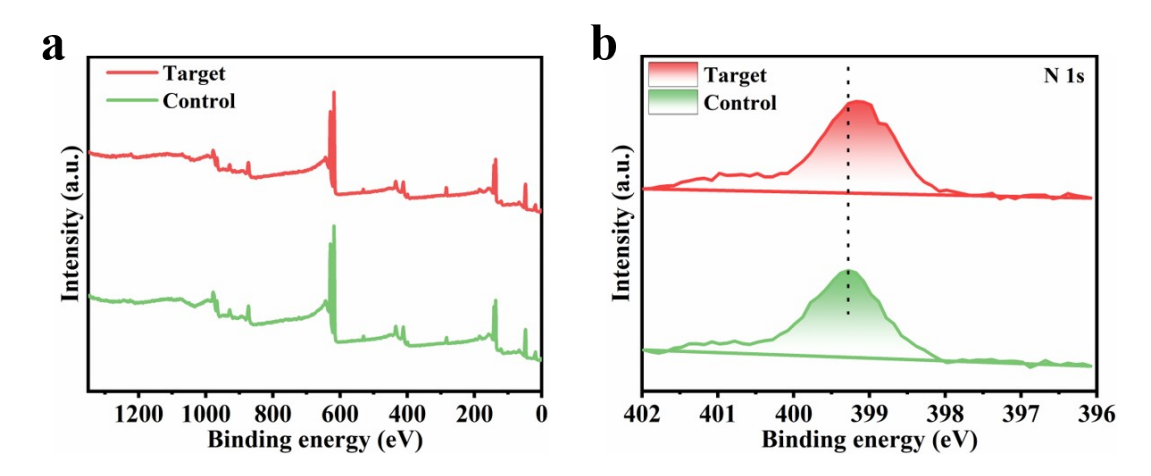


Fig. S15 Full XPS spectra (a) and N 1s XPS core spectra (b) of different perovskite films.

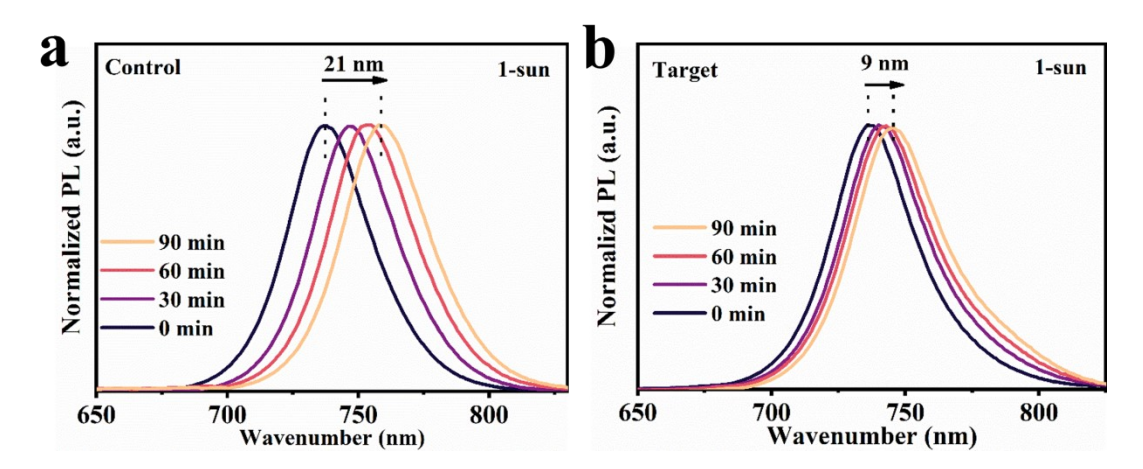


Fig. S16 The evolution of the normalized PL spectra of the (e) *Control* and (f) *Target* perovskite films under one-sun illumination at 25°C within 90 min.

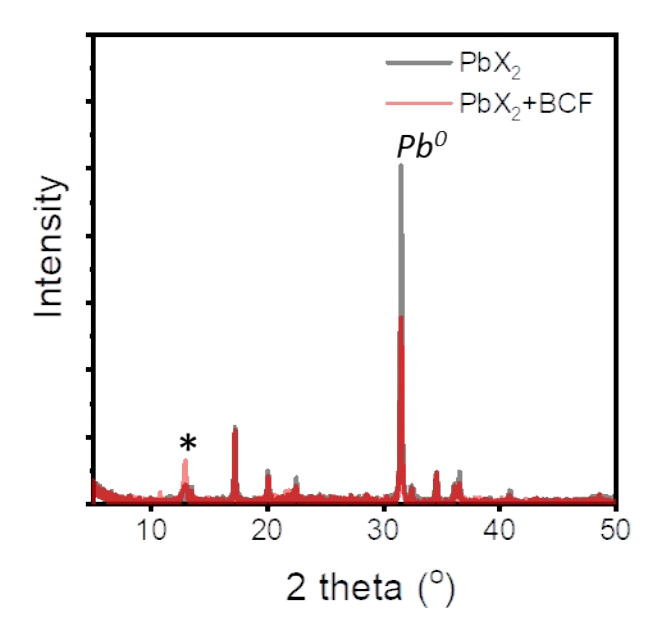


Fig. S17. Comparison of the XRD patterns of the aged PbX_2 and PbX_2+BCF films evidences stabilizing effect of BCF as can be concluded from almost twice lower intensity of ${}^{0}Pb$ peak. The I:Br content in PbX_2 was 3:1. Aging conditions: 100 mW/cm², 77±3 ${}^{\circ}C$, pure nitrogen atmosphere, 36 h.

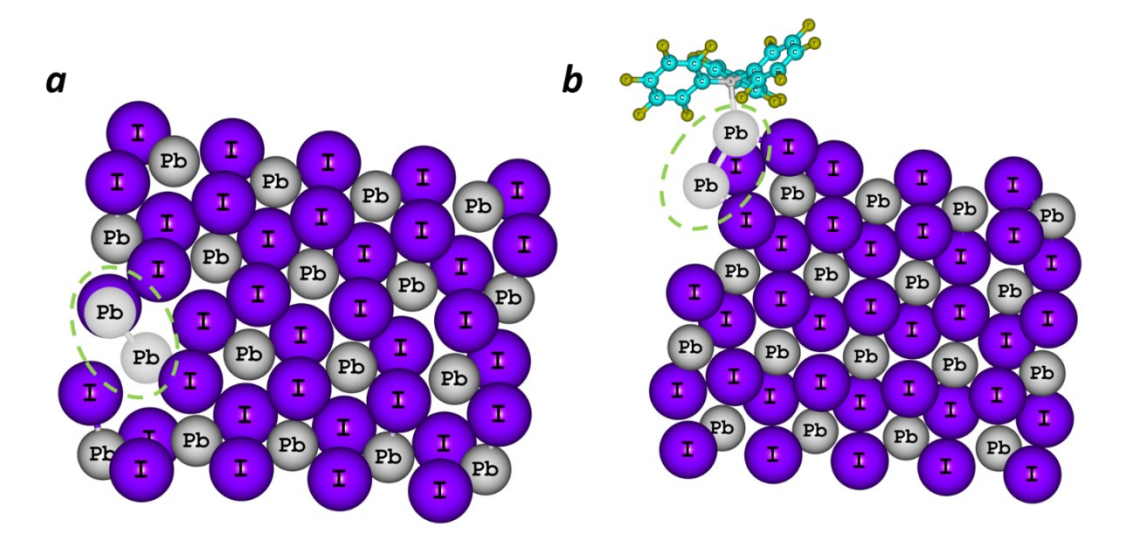


Fig. S18. (a) The model PbI_2 cluster with a single introduced Pb^0 atom paring with a Pb^{2+} cation (marked with olive dashed line). (b) BCF binding to the Pb^0 atom localized on the PbX_2 surface.

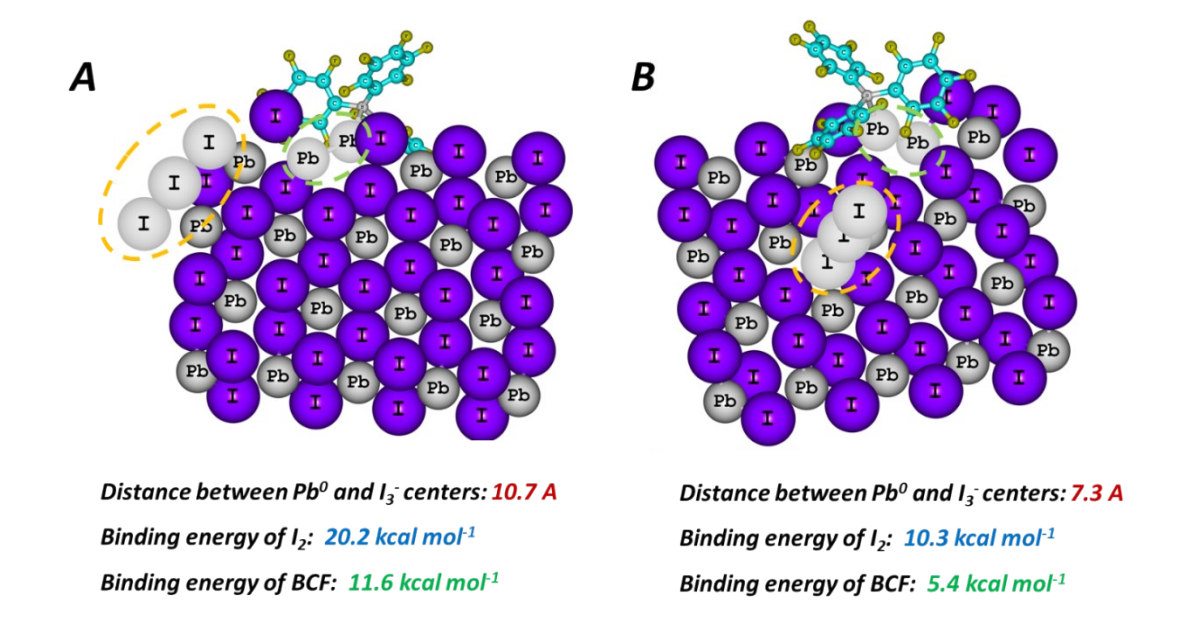


Fig. S19. Two representative structures of PbX₂ with the photogenerated Pb⁰ and I_3 -species placed at different distances. I_2 and BCF binding energies dramatically decrease when Pb⁰ and I_3 -centers are localized closer to each other in the structure B.

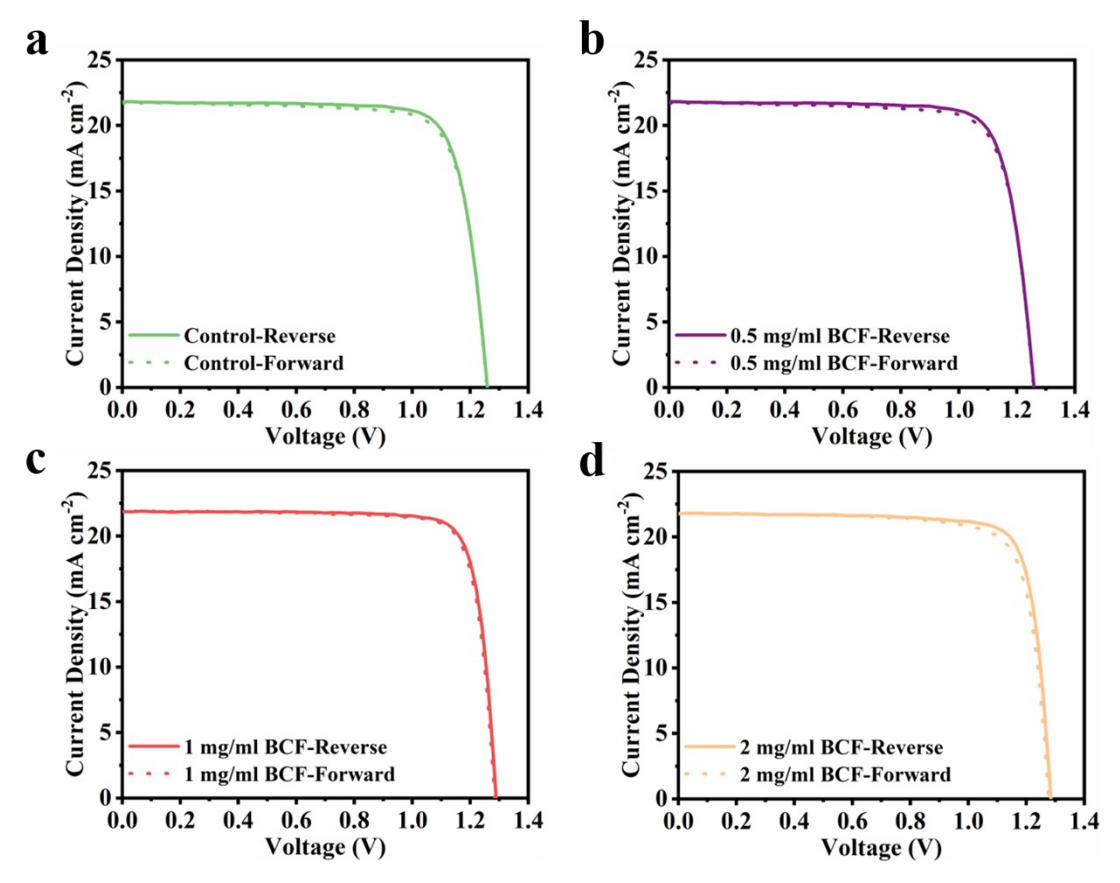


Fig. S20 The forward and reverse sweep J-V curves of the best-performance devices with the differently processed perovskite absorber films.

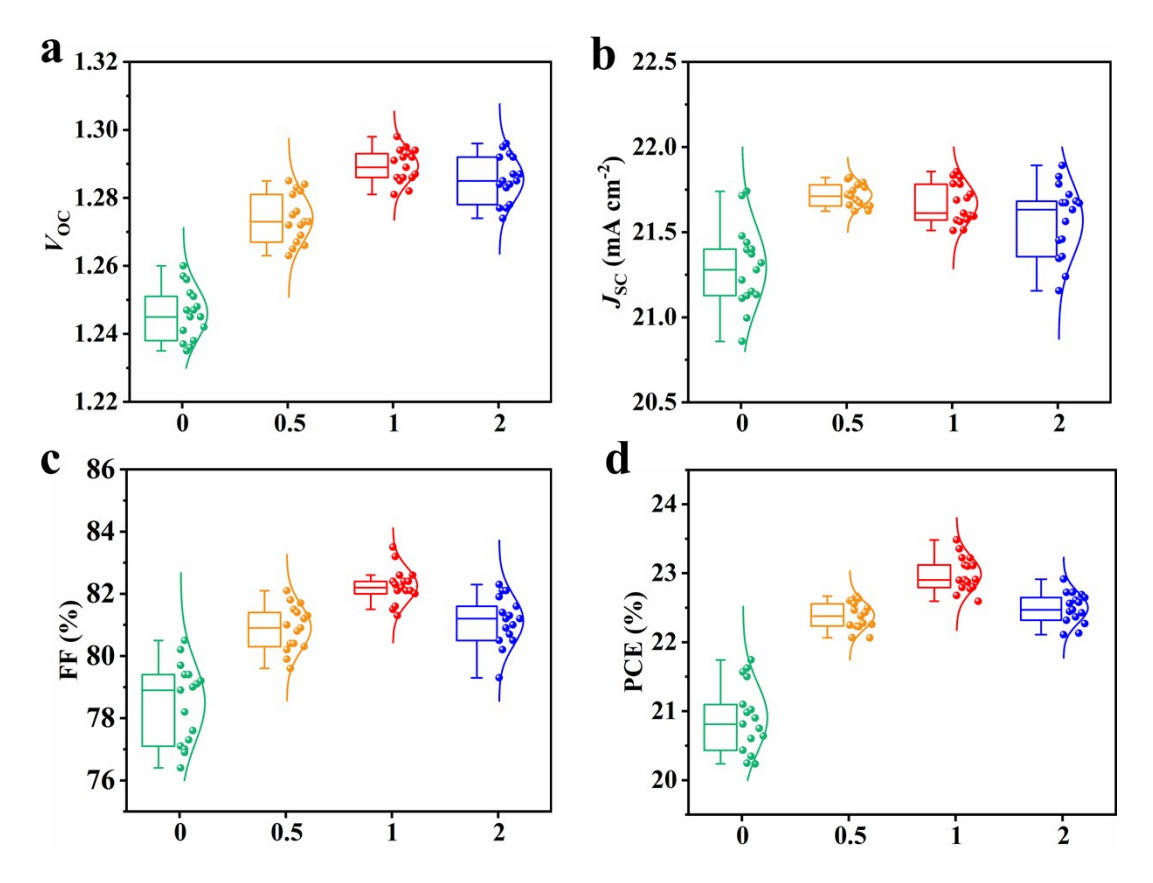


Fig. S21 The influence of different concentrations (mg/ml) of BCF on the performance of 1.68 eV perovskite solar cells (statistics from 16 individual devices in each batch).

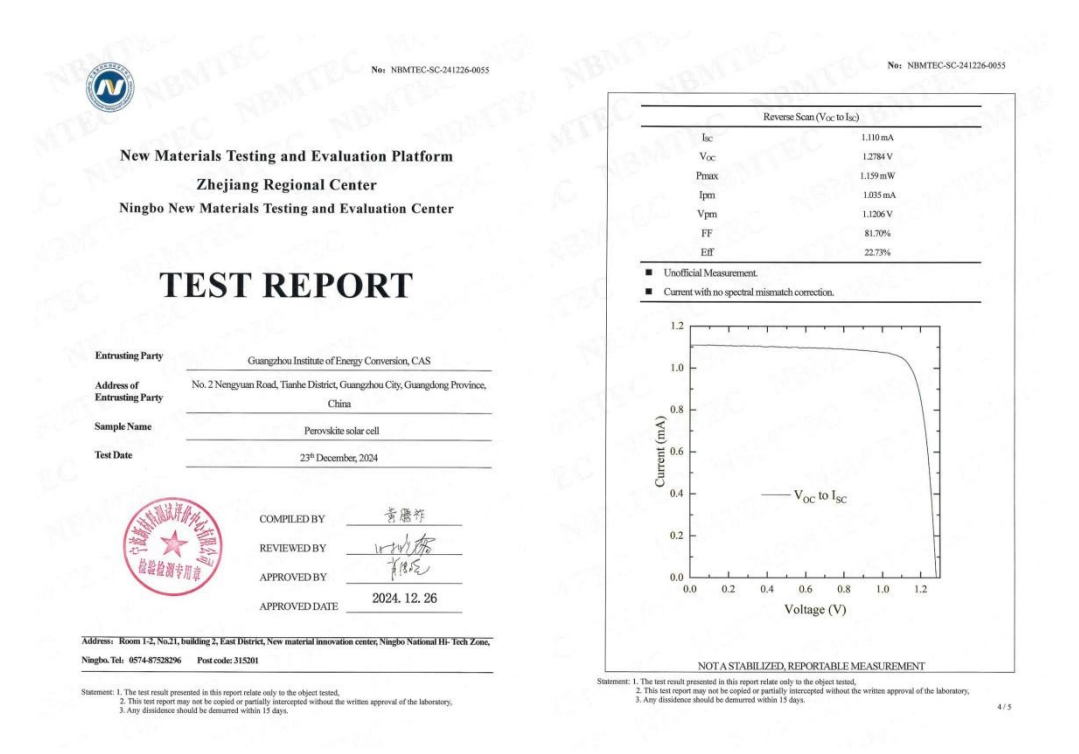


Fig. S22 The certified result for a perovskite solar cell with a PCE of 22.73% provided by Ningbo New Materials Testing and Evaluation Center.

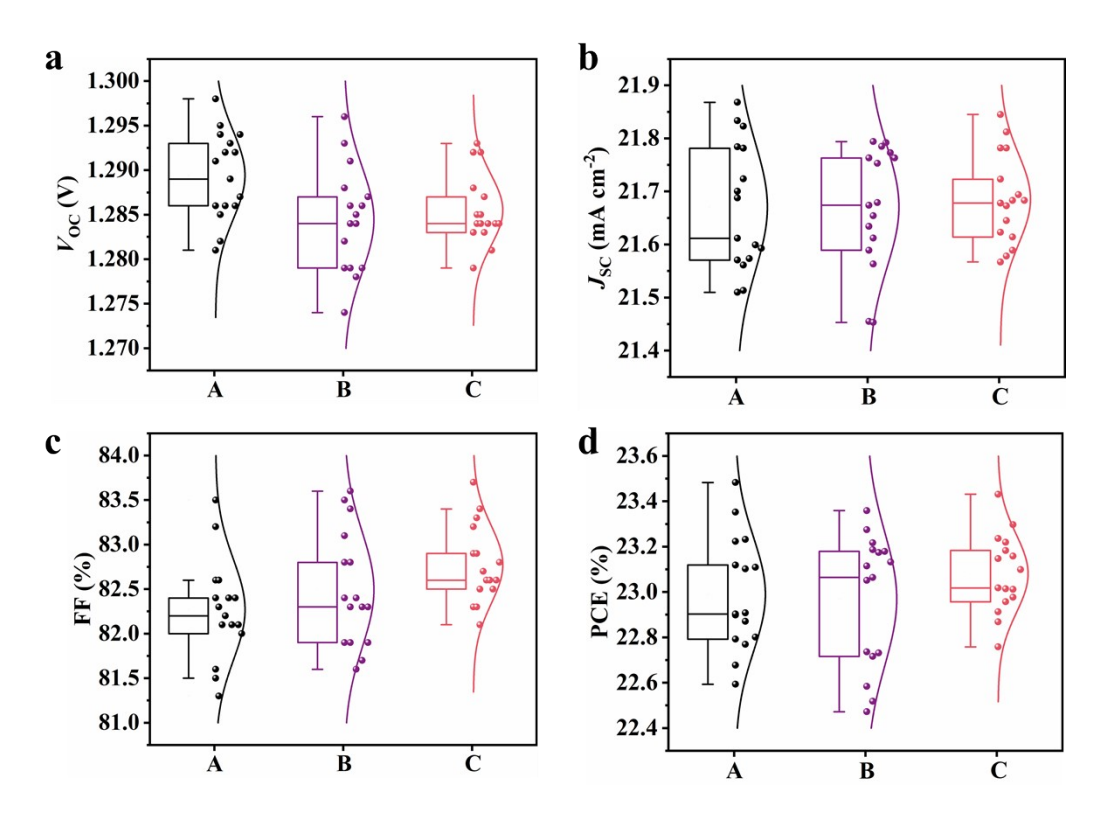


Fig. S23 The performance of the three different batches of devices prepared with PbI₂ received from different companies (each batch consists of 16 individual devices).

A, B and C represented the three different companies that purchased PbI₂, (the purity of PbI₂ is 99.999%, 99.999%, and 99.99% respectively).

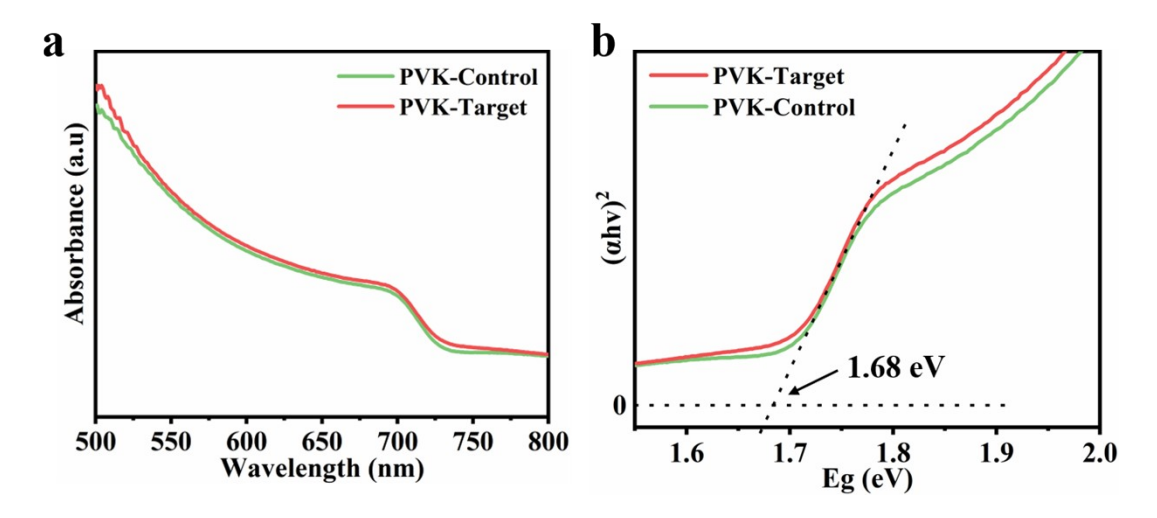


Fig. S24 UV-vis absorption spectroscopy (a) and the optical bandgaps (b) of different perovskite films.

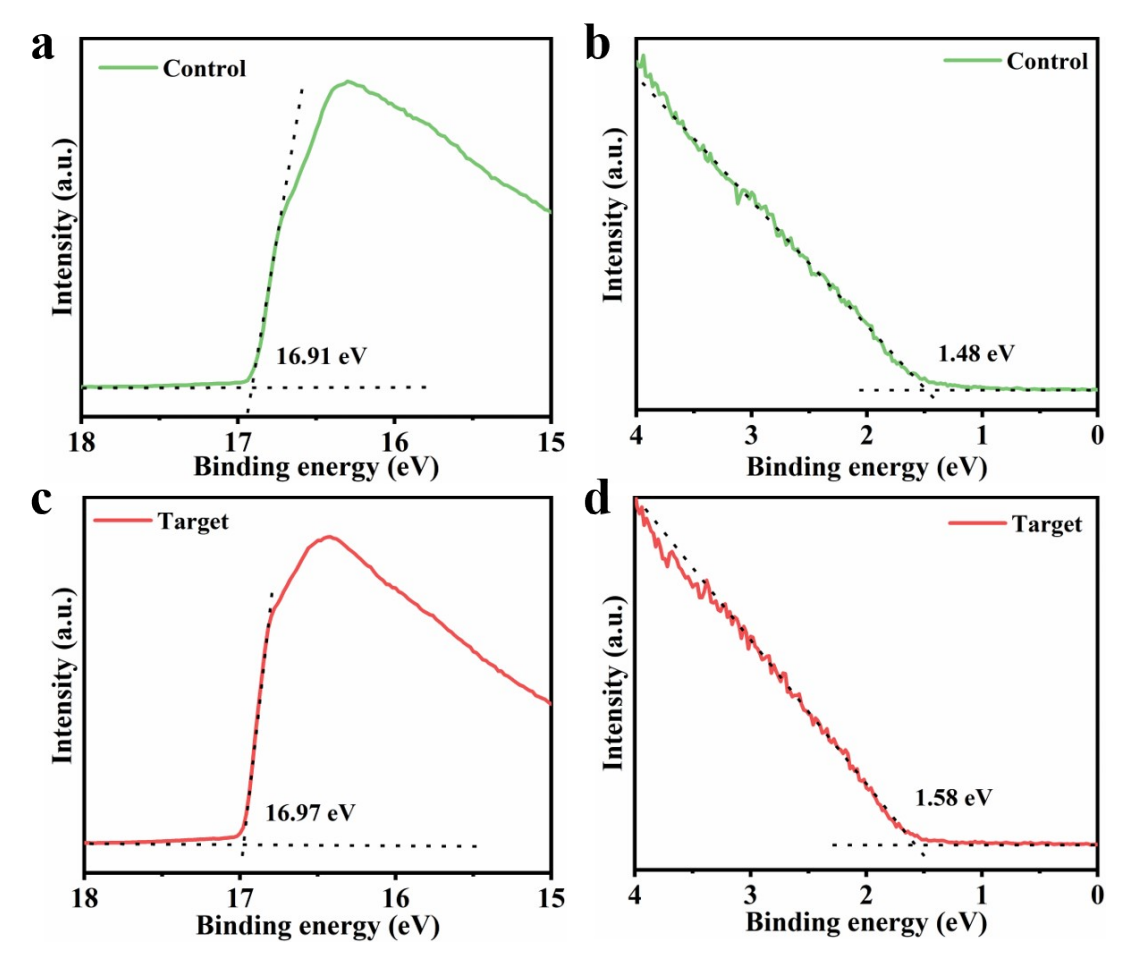


Fig. S25 The secondary-electron cut-off binding energy (a, c) and the valence band region (b, d) of different perovskite films.

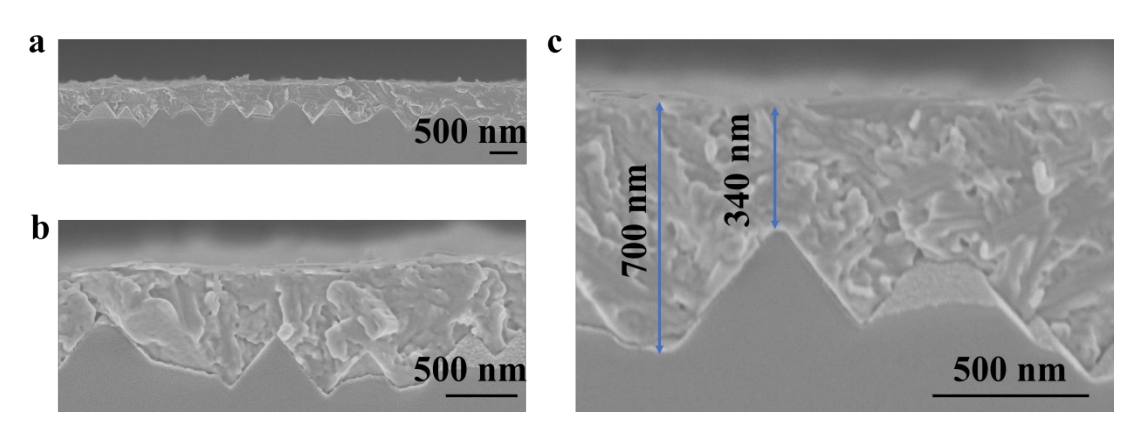


Fig. S26 Cross-sectional SEM images of PbX₂/Si stack shown in different scales.

Table S1 Fast and slow components of the PL decay curves and their corresponding ratios for differently processed perovskite films.

Samples	$\mathbf{A_1}$	τ ₁ (ns)	\mathbf{A}_2	τ ₂ (ns)	τ _{ave} (ns)
Control	0.020	12.13	0.980	731.49	731.25
Target	0.0035	17.64	0.9965	1108.76	1108.70

Equations S1

Detailed TRPL fitting results are fitted using a dual exponential decay function model, according to the following equation:

$$\frac{t}{I(t) = I_0 + A_1 \exp(-\tau_1) + A_2 \exp(-\tau_2)}$$

Equations S2

 τ_{ave} can be calculated by the equation:

$$\tau_{ave} = \frac{{A_1 * \tau_1}^2 + {A_2 * \tau_2}^2}{{A_1 * \tau_1} + {A_2 * \tau_2}}$$

Equations S3

Internal QFLS can be calculated based on the relationship with PLQY according to following equation:

 $QFLS = QFLS_{rad} + k_BT \ln(PLQY)$

Table S2PLQY and QFLS results of control and BCF perovskute films without or with ETL on glass, respectively.

Structure	Sample	PLQY (%)	QFLS (eV)
GLASS/PVK	Control	2.544	1.306
	Target	3.602	1.315
GLASS/PVK/ETL	Control	0.522	1.265
	Target	1.867	1.298

Table S3

The defect density (N_{trap}) and the limit filling voltage (V_{TFL}) of the device.

Samples	$V_{ m TFL}/{ m V}$	$N_{\rm trap}/{\rm cm}^{-3}$
Control	0.467	6.73×10 ¹⁵
Target	0.278	4.01×10 ¹⁵

Equations S4

The relationship between the defect density (N_{trap}) and the limit filling voltage (V_{TFL}) of the device is shown as follows equation:

$$N_{ ext{trap}} = rac{2arepsilon_0 arepsilon_{rV_{TFL}}}{qL^2}$$

where ε_0 means the vacuum permittivity, ε_r means the dielectric constant of perovskite, V_{TFL} means the onset voltage of the TFL region, q means the elementary charge, and L means the perovskite film thickness.

Table S4 Performance summary for the champion devices assembled using different concentrations of BCF.

Samples	Scanning	$V_{\rm OC}$	FF	Jsc	PCE
Samples	direction	(V)	(%)	(mA cm ⁻²)	(%)
Control	Reverse	1.257	79.7	21.71	21.74
	Forward	1.257	78.4	21.71	21.41
BCF-0.5 mg	Reverse	1.285	81.0	21.82	22.70
	Forward	1.281	80.2	21.86	22.45
BCF-1 mg	Reverse	1.291	83.2	21.87	23.49
	Forward	1.285	82.4	21.91	23.21
BCF-2 mg	Reverse	1.284	81.9	21.78	22.914
	Forward	1.277	79.3	21.83	22.109

Table S5 Performance summary for the devices assembled using different concentrations of BCF (statistics from 16 individual devices in each batch).

Samples (BCF)		$V_{\rm OC}\left({ m V}\right)$	FF (%)	Jsc (mA cm ⁻²)	PCE (%)
Control (0)	Best	1.257	79.7	21.71	21.74
	Average	1.246 ± 0.008	78.5 ± 1.3	21.30 ± 0.24	20.91±0.50
0.5 mg/ml	Best	1.285	81.0	21.82	22.70
	Average	1.274 ± 0.007	80.9 ± 0.7	21.72 ± 0.07	22.39±0.2
Torget (1)	Best	1.291	83.2	21.87	23.49
Target (1)	Average	1.289 ± 0.005	82.2 ± 0.5	21.67 ± 0.12	22.99±0.25
2 mg/ml	Best	1.284	81.9	21.78	22.91
	Average	1.285±0.007	81.1±0.8	21.57±0.21	22.50±0.23

Equations S5

the dependence studies of $V_{\rm OC}$ with various light intensities ranging from 10 to 100 mW cm⁻², and calculated the ideality factor ($n_{\rm id}$) according to equation:

$$V_{\rm OC} = \frac{n_{id}k_BT}{q}\ln(I) + B$$

where $k_{\rm B}$ symbolizes the Boltzmann constant, T symbolizes thermodynamic temperature, q symbolizes the electron charge, I symbolize light intensity and B is constant, respectively.

Table S6 Summary on the photovoltaic parameters of inverted 1.68 eV wide-bandgap PSCs extracted from recent literature on all PSCs.

Year	Eg(eV)	$V_{\rm OC}({ m V})$	FF(%)	$J_{\rm SC}({ m mA~cm}^{-2})$	PCE(%)	Ref.
2023	1.68	1.239	82.50	21.16	21.63	[11]
2023	1.68	1.26	81.6	21.60	22.19	[12]
2023	1.68	1.248	84.4	20.82	21.93	[13]
2023	1.68	1.28			21.5	[14]
2024	1.68	1.216	82.73	22.18	22.35	[15]
2024	1.68	1.275	84.83	21.68	23.45	[16]
2025	1.68	1.291	83.2	21.87	23.49	This work

Table S7 Summary on the photovoltaic parameters of inverted wide-bandgap (>1.63 eV) PSCs prepared via the all-solution two-step method extracted from recent literature on all PSCs.

Year	Eg(eV)	$V_{\rm OC}({ m V})$	FF(%)	$J_{\rm SC}({ m mA~cm^{-2}})$	PCE(%)	Ref.
2022	1.63	1.20	80.4	21.82	21.02	[17]
2025	1.68	1.291	83.2	21.87	23.49	This work

Table S8 Performance summary for three different batches of devices prepared with PbI₂ from different companies (16 individual devices in each batch).

Samples (BCF)		$V_{\rm OC}\left({ m V}\right)$	$V_{\rm OC}\left(\mathrm{V}\right)$ FF (%)		PCE (%)
Best		1.292	83.1	21.86	23.48
A Average 1.289 ± 0.00	1.289 ± 0.005	82.3 ± 0.6	21.66 ± 0.13	23.0±0.25	
Best B Average	1.287	83.4	21.76	23.36	
	Average	1.284 ± 0.006	82.5 ± 0.6	21.67 ± 0.11	22.97±0.29
C	Best	1.283	83.6	21.85	23.43
С	Average	1.286 ± 0.004	82.8±0.4	21.69±0.08	23.08±0.17

A, B and C represented the three different companies that purchased PbI₂.

Table S9 Summary on $E_{\rm VBM}$ and $E_{\rm CBM}$ energies of differently prepared perovskite absorber films.

Samples	E_{VBM} (eV)	$E_{\mathrm{CBM}}\left(\mathrm{eV}\right)$	$E_{\rm F}\left({ m eV}\right)$
Control	-5.79	-4.11	-4.31
Target	-5.83	-4.15	-4.25

Table S10 The best-performing photovoltaic parameters of perovskite/Si TSCs without or with BCF modified.

Samples		$V_{\mathrm{OC}}\left(\mathbf{V}\right)$	FF (%)	Jsc (mA cm ⁻²)	PCE (%)
Target	Reverse	1.940	79.2 20.265		31.12
	Forward	1.934	79.1	20.325	31.09
Control	Reverse	1.889	77.3	20.01	29.22
	Forward	1.882	77.1	20.113	29.18

Table S11 Summary on the photovoltaic parameters of perovskite/Si TSCs prepared by two-step method extracted from recent literature on all PSCs.

Year	method	V _{oc} (V)	FF (%)	$J_{SC} ({ m mA~cm}^{-2})$	PCE (%)	Ref.
2024	evaporation - solution	1.83	78.63	20.45	29.4	[18]
2025	evaporation - solution	1.895	79.1	20.3	30.5	[19]
2025	evaporation - solution	1.945	78.38	20.22	30.83	[20]
2025	all-solution	1.940	79.2	20.265	31.12	This work

References

- [1] Kresse, G.; Hafner, J. Ab Initio Molecular-Dynamics Simulation of the Liquid-Metalamorphous- Semiconductor Transition in Germanium. *Physical Review B* 1994, 49 (20), 14251–14269. https://doi.org/10.1103/PhysRevB.49.14251.
- [2] Perdew, J. P.; Burke, K.; Ernzerhof, M. Generalized Gradient Approximation Made Simple. *Physical Review Letters* 1996, 77 (18), 3865–3868. https://doi.org/10.1103/PhysRevLett.77.3865.
- [3] Grimme, S.; Antony, J.; Ehrlich, S.; Krieg, H. A Consistent and Accurate Ab Initio Parametrization of Density Functional Dispersion Correction (DFT-D) for the 94 Elements H-Pu. *Journal of Chemical Physics* 2010, *132* (15), 154104. https://doi.org/10.1063/1.3382344.
- [4] Blöchl, P. E. Projector Augmented-Wave Method. *Physical Review B* 1994, *50* (24), 17953–17979. https://doi.org/10.1103/PhysRevB.50.17953.
- [5] Kresse, G.; Joubert, D. From Ultrasoft Pseudopotentials to the Projector Augmented-Wave Method. *Physical Review B* 1999, *59* (3), 1758–1775. https://doi.org/10.1103/PhysRevB.59.1758.
- [6] Płowaś-Korus, I.; Kaczkowski, J. Comparative Density Functional Studies of BiMO₃ Polymorphs (M = Al, Ga, In) Based on LDA, GGA, and Meta-GGA Functionals. *New Journal of Chemistry* 2022, 46 (32), 15381–15391. https://doi.org/10.1039/D2NJ03258A.
- [7] D. N. Laikov. Chem. Phys. Lett. 1997, 281, 151
- [8] J. P. Perdew, K. Burke, M. Ernzerhof. *Phys. Rev. Lett.* **1996**, 77, 3865.
- [9] W. J. Stevens, H. Bash, M. Krauss. J. Chem. Phys. 1984, 12, 6026.
- [10] D. N. Laikov, Chem. Phys. Lett., 2005, 416, 116.
- [11] N. Yan, Y. Gao, J. Yang, Z. Fang, J. Feng, X. Wu, T. Chen, S. Liu, Wide-Bandgap Perovskite Solar Cell Using a Fluoride-Assisted Surface Gradient Passivation Strategy. Angewandte Chemie International Edition. 2023, 62 (11).
- [12]Z. Song, J. Yang, X. Dong, R. Wang, Y. Dong, D. Liu, Y. Liu, Inverted Wide-Bandgap 2D/3D Perovskite Solar Cells with >22% Efficiency and Low Voltage Loss.

Nano Letters. 2023, 23 (14), 6705-6712.

[13] E. Aydin, E. Ugur, B.K. Yildirim, T.G. Allen, P. Dally, A. Razzaq, F. Cao, L. Xu, B. Vishal, A. Yazmaciyan, A.A. Said, S. Zhumagali, R. Azmi, M. Babics, A. Fell, C. Xiao, S. De Wolf, Enhanced optoelectronic coupling for perovskite/silicon tandem solar cells. Nature. 2023, 623 (7988), 732-738.

[14] S. Mariotti, E. Köhnen, F. Scheler, K. Sveinbjörnsson, L. Zimmermann, M. Piot, F. Yang, B. Li, J. Warby, A. Musiienko, D. Menzel, F. Lang, S. Keßler, I. Levine, D. Mantione, A. Al-Ashouri, M.S. Härtel, K. Xu, A. Cruz, J. Kurpiers, P. Wagner, H. Köbler, J. Li, A. Magomedov, D. Mecerreyes, E. Unger, A. Abate, M. Stolterfoht, B. Stannowski, R. Schlatmann, L. Korte, S. Albrecht, Interface engineering for high-performance triple-halide perovskite–silicon tandem solar cells. Science. 2023, 381, 63-69.

[15] L. Yang, Z. Fang, Y. Jin, H. Feng, B. Deng, L. Zheng, P. Xu, J. Chen, X. Chen, Y. Zhou, C. Shi, W. Gao, J. Yang, X. Xu, C. Tian, L. Xie, Z. Wei, Suppressing Halide Segregation via Pyridine-Derivative Isomers Enables Efficient 1.68 eV Bandgap Perovskite Solar Cells. Advanced Materials. 2024, 36 (21).

[16] Z. Li, A. Sun, C. Tian, R. Zhuang, Y. Zheng, X. Wu, B. Ouyang, J. Du, J. Cai, J. Chen, T. Xue, R. Li, T. Cen, Y. Zhao, K. Zhao, Q. Chen, C.-C. Chen, Sustainable Molecular Passivation via Heat-Induced Disaggregation and Redox Reactions for Inverted Perovskite Solar Cells. ACS Energy Letters. 2024, 9 (11), 5471-5482.

[17]B. Chen, P. Wang, R. Li, N. Ren, W. Han, Z. Zhu, J. Wang, S. Wang, B. Shi, J. Liu, P. Liu, Q. Huang, S. Xu, Y. Zhao, X. Zhang, A Two-Step Solution-Processed Wide-Bandgap Perovskite for Monolithic Silicon-Based Tandem Solar Cells with >27% Efficiency. ACS Energy Letters. 2022, 7 (8), 2771-2780.

[18] X. Zheng, W. Kong, J. Wen, J. Hong, H. Luo, R. Xia, Z. Huang, X. Luo, Z. Liu, H. Li, H. Sun, Y. Wang, C. Liu, P. Wu, H. Gao, M. Li, A. Bui, Y. Mo, X. Zhang, G. Yang, Y. Chen, Z. Feng, H.T. Nguyen, R. Lin, L. Li, J. Gao, H. Tan, Solvent engineering for scalable fabrication ofperovskite/silicon tandem solar cells in air. Nature Communications. 2024, 15:4907.

[19] H. Luo, X. Han, B. Yang, W. Ou, J. Suo, H. Sun, X. Zheng, J. Hong, Z. Chu, L.

Zhao, S. Yang, P. Wu, C. Duan, C. Liu, M. Li, L. Li, R. Lin, W. Kong, H. Tan, Damp-Stable Perovskite/Silicon Tandem Solar Cells with Internal Encapsulating SulfoniumBased Molecules. ACS Energy Letters. 2025, 10, 3325–3334.

[20] B. Shi, P. Liu, Z. Sunli, W. Han, C. Sun, Y. Liu, Y. Luo, J. Si, P. Du, F. Zhang, M. Yang, Y. He, B. He, D. Zhang, X. Du, X. Xu, R. Xia, X. Zhang, Y. Chen, J. Gao, Y. Zhao, X. Zhang, Halogen anion pre-homogenization of sequentially deposited wide bandgap perovskites for commercial textured perovskite/silicon tandem solar cells. Energy & Environmental Science. 2025, 18, 6297–6306.